physica status solidi (RRL) – Rapid Research Letters

RESEARCH ARTICLE

Thermal Evolution of Excitons and Defect-Localized States in Monolayer 2H-$MoTe_2$

Aksa Thomas[1,2] | Aditya Singh[1] | Satinder K. Sharma[2] | Ajay Soni[1]

[1]School of Physical Sciences, Indian Institute of Technology Mandi, Mandi, India | [2]School of Computing & Electrical Engineering, Indian Institute of Technology Mandi, Mandi, India

Correspondence: Ajay Soni (ajay@iitmandi.ac.in)

Received: 27 November 2025 | **Revised:** 30 December 2025 | **Accepted:** 5 January 2026

Keywords: exciton–phonon coupling | excitons | monolayer 2H-$MoTe_2$ | photoluminescence spectroscopy

ABSTRACT

A monolayer of hexagonal molybdenum ditelluride (2H-$MoTe_2$), characterized by strong spin–orbit coupling and a relatively small energy gap (1.1 eV), is highly promising for valleytronics and excitonic device applications. In this work, we investigate the temperature-dependent evolution of exciton complexes in monolayer 2H-$MoTe_2$ using temperature-dependent photoluminescence (PL) spectroscopy, complemented by excitation power-dependent measurements. We clearly identify neutral exciton ($A_{1s} \sim 1.19$ eV) and trion ($A^- \sim 1.162$ eV) states and systematically analyze their temperature-dependent shifts using both the semi-empirical model and the Varshni relation. Additionally, we observe an additional peak at ~1.132 eV, attributed to a localized defect-bound excitonic state, supported by excitation power-dependent PL analysis. These results provide important insights into defect-induced modifications of the excitonic fine structure and deepen our understanding of exciton dynamics in this two-dimensional semiconductor.

1 | Introduction

Research on two-dimensional (2D) materials witnessed an exponential surge following the exfoliation of monolayer graphene in 2004 [1, 2]. Since then, the field has rapidly evolved, extending beyond graphene to encompass a diverse class of layered materials, most notably the transition metal dichalcogenides (TMDCs) [3, 4], with the chemical formula MX_2 (M = Mo, W, X = S, Se, Te). The TMDCs are known for the tunable bandgap owing to the flexibility in varying thickness, the choice of chalcogen atoms, and alloying together with changing stoichiometric ratios of chalcogen as well as transition metal atoms. As we reduce the dimensionality down to monolayer, the quantum confinement effects and weak dielectric screening yield a direct bandgap presumably at $K^{\pm}$ points of the hexagonal Brillouin zone as in case of 2H hexagonal crystal structure. The monolayer exhibits a valley degree of freedom resulting from broken inversion symmetry combined with C_3 rotational symmetry, leading to lowest energy excitonic states that are twofold degenerate and governed by contrasting chiral optical selection rules. Spin-valley locking in monolayer TMDCs arises from strong coupling between the spin and valley degrees of freedom, such that each valley is intrinsically associated with a unique spin polarization [5]. Owing to spin-valley locking and broken inversion symmetry, the optical selection rules in monolayer TMDCs become both valley- and spin-dependent, whereby specific circular polarizations (σ^+ or σ^-) of light selectively excite electronic transitions in distinct valleys with corresponding spin orientations [6]. The helicity of the incident circularly polarized light determines the initialization of carriers with a specific valley and spin index, reflecting the inherent coupling between spin and valley degrees of freedom in the system [7]. This mechanism enables precise optical control of spin and valley pseudospins, underpinning phenomena forming the basis of valley polarization, spin-polarized photocurrents, and emerging valleytronic devices and materials engineering [8, 9]. The exceptionally strong light–matter interaction enables monolayer TMDCs at the forefront of the next-generation optoelectronics, valleytronics, and flexible quantum device applications. Optical properties in the monolayer TMDCs are primarily

governed by the rich excitonic physics. Excitons are photogenerated quasi-particles that are a bound pair of electrons and holes held together by a strong Coulombic force. Excitons in monolayer TMDCs, characterized by high binding energies and large oscillator strengths, provide an ideal platform to explore a wide range of condensed matter phenomena, including Mott insulators, Wigner crystals, and light-induced magnetic phases, through optical spectroscopy [10].

In the family of TMDCs, monolayer hexagonal molybdenum ditelluride (2H-$MoTe_2$) with an approximate bandgap of ~1.1 eV is notable for its substantial spin–orbit coupling (SOC) and high exciton binding energy [11–13]. It has the smallest among the Mo-based TMDCs that emit near the silicon band edge making it an attractive platform for silicon-compatible optoelectronics and telecom-band photonics. So, a fundamental understanding of photo physics is essential for 2D electronics. 2H-$MoTe_2$ exhibits a thickness-dependent Raman spectrum and is theoretically predicted to possess a room-temperature carrier mobility exceeding that of MoS_2 that is phonon-limited [14]. The dominant PL emission originates from a direct transition involving exciton and trion recombination. Investigations on exceptionally high-quality TMDC samples have identified the presence of Rydberg excitons that are excited states analogous to hydrogenic energy levels and have been explored in monolayer 2H-$MoTe_2$ [11, 15–20]. Owing to the existence of heavy tellurium atoms, $MoTe_2$ exhibits significantly stronger spin–orbit effects (~230 meV in the valence band and ~50 meV in the conduction band) and a more pronounced bright–dark A-exciton splitting (~34 meV) in comparison with other Mo-based TMDCs [21]. Besides the neutral and charged excitonic peaks, PL spectra at low temperatures often show an additional feature ascribed to localized excitons rather than free excitons. Although this feature is predominantly associated to defects in TMDCs, several questions regarding its exact nature remain unresolved. Neutral excitons are generally mobile but both neutral and charged lattice defects can trap electron–hole pairs and form bound excitons. The definite binding energy between neutral exciton and a defect results in a defect-bound exciton peak in the PL spectrum at an energy slightly lower than the neutral exciton peak. The temperature-dependent study of the defect-bound excitons reveals their degree of localization at the defect sites and their interaction with the surrounding lattice environment. These defect-bound excitons are more prominent at cryogenic temperatures, where they exhibit sharp spectral features due to strong localization, thereby enabling precise measurements. The presence of a defect-bound exciton state at an energy lower than the free exciton peak is further confirmed through laser power-dependent PL measurements at 3 K. Its distinct temperature-dependent behavior and the disappearance of this feature above 40 K clearly indicate strong localization at defect sites. Understanding their dynamics at low temperatures is therefore essential for guiding defect-engineering strategies aimed at optimizing light emission, photodetection, and quantum photonic applications, including stable single-photon sources and tunable excitonic devices.

2 | Results and Discussions

2.1 | XRD

The X-ray diffraction (XRD) pattern (Figure 1a) of 2H-$MoTe_2$ confirms the phase purity with all the diffraction peaks consistent with the existing literature [22]. The lattice parameters estimated from Rietveld refinement are $a = b \sim 3.52$ Å, and $c \sim 13.96$ Å with the space group $P6_3/mmc$. The crystal structure as shown in Figure 1b consists of two triatomic layers (Te–Mo–Te) coupled with a weak van der Waals (vdw) force along the c-axis. The unit cell of bulk 2H-$MoTe_2$ consists of six atoms and exhibits 18 vibrational modes at the Brillouin zone center (15 optical modes and 3 acoustic modes) with the irreducible representations of phonon modes at Γ point given by $\Gamma_{bulk} = 2E_u^1(IR) + 2E_{2g}(R) + E_{2u} + E_{1g}(R) + A_{2u}(IR) + 2B_{2g} + B_{1u} + A_{1g}(R)$ and $\Gamma_{monolayer} = 2E'(R + IR) + E''(R) + 2A_2''(IR) + A_1'(R)$ [17, 23, 24].

2.2 | Raman Spectroscopy

The room temperature Raman spectra of the bulk 2H-$MoTe_2$ are shown in Figure 2a with prominent modes present at ~170 cm^{-1} (out-of-plane A_{1g} mode) and at ~234 cm^{-1} (in-plane E_{2g}^1) [11]. The phonon modes at ~143.8 cm^{-1} (2TA (M)), 185 cm^{-1} (E_{2g}^1 (M) – LA (M)), 202 cm^{-1} (2LA (M)), 327.6 cm^{-1} ($2A_{1g}$ (M)),

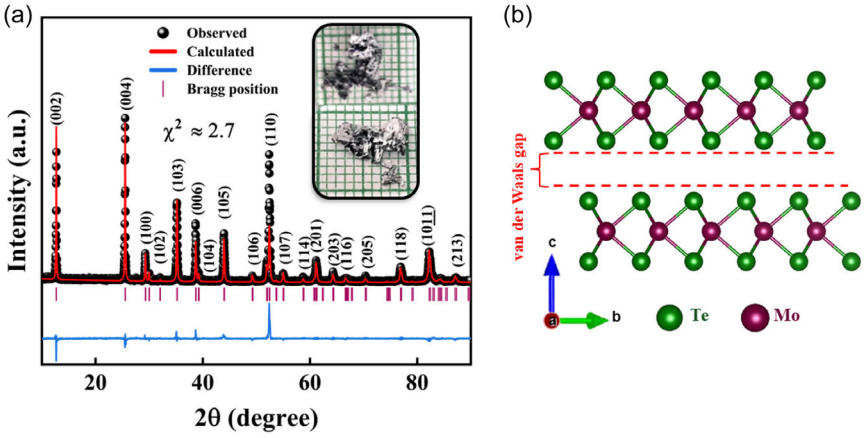

FIGURE 1 | (a) Powder X-ray diffraction pattern of 2H-$MoTe_2$; the inset shows the photograph of the grown crystal. (b) Side view of the unit cell of the layered crystal structure of 2H-$MoTe_2$, with the van der Waals gap.

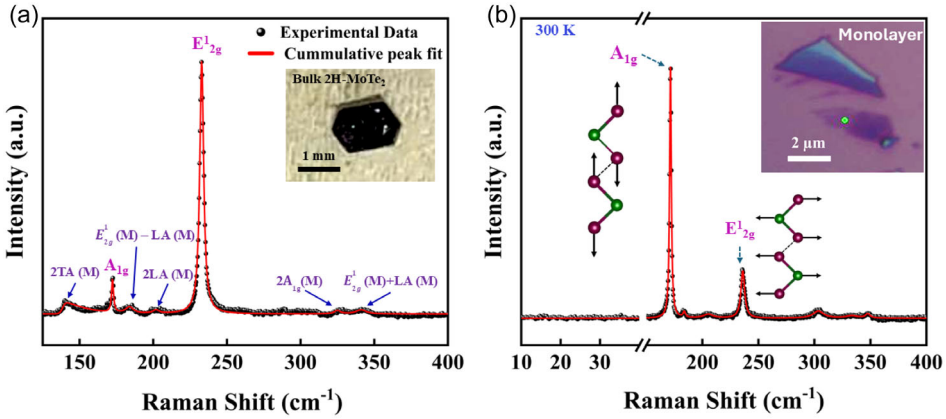

FIGURE 2 | (a) Raman spectra of bulk 2H-$MoTe_2$ at room temperature fitted with Lorentzian function and the inset shows the optical image of the hexagonal crystal. (b) Raman spectra of monolayer 2H-$MoTe_2$ and inset shows the optical image of the monolayer on SiO_2/Si substrate.

and 341.8 cm^{-1} (E^1_{2g} (M) + LA (M)) are activated because of the double resonance process at the M point of the Brillouin zone, induced by excitation with the resonant laser of energy 1.96 eV [25]. In order to investigate the excitonic physics behavior in the monolayer, thin flakes are mechanically exfoliated from the bulk 2H-$MoTe_2$ as described in the experimental section. Room temperature Raman spectra of the exfoliated 2H-$MoTe_2$ flake is shown in Figure 2b, which confirms monolayer by the relative intensity ratio between the A_{1g} (at ~171 cm^{-1}) mode and E^1_{2g} (at ~236 cm^{-1}) mode as well as the absence of interlayer shear and breathing modes in the low-frequency regime [11, 26, 27].

2.3 | Photoluminescence Spectroscopy

To study the exciton dynamics in monolayer 2H-$MoTe_2$, temperature-dependent PL is performed from 3 to 300 K. The PL spectra at 3 K is shown in Figure 3a with the energy level diagram in the inset [13, 15, 20, 28–30]. We observe A_{1s} exciton and A^- trion peaks at approximately at ~1.19 eV and at ~1.16 eV, respectively [15, 18, 20, 23, 29, 30], while additional optical transitions at about ~1.132 and 1.157 eV emerge from an unknown origin and require further analysis [18]. The schematic of the possible origins of the observed emissions is explained from the energy band diagram in Figure 3b, which depicts the K^+ and K^- valleys of the monolayer 2H-$MoTe_2$, thus showing the intrinsic valence band and potentially conduction band splitting [21]. To understand further on the existence and evolution of exciton dynamics, we performed the temperature-dependent PL measurements and all the spectra are presented in the supplementary information (Figure S1). The PL above ~160 K are not sharp as the background noise is large. To understand the contribution from the substrate, temperature-dependent PL has been done with similar experimental parameters and compared with sample spectra (Figure S2). Above 160 K, the contribution from the substrate is more prominent as compared to the monolayer. Thus, we focused on the spectra until 160 K for understanding of the PL emissions.

Figure 4a shows the PL spectra recorded from 3 to 160 K, where the trion peak intensity progressively decreases and it disappears at 100 K. The reduction in the trion intensity is attributed to dissociation of trions into free excitons and thermally generated excess charge carriers in the sample [18, 29]. Above160 K, exciton peak also weakens, primarily due to its relatively small binding energy and because the corresponding emission energy shifts beyond the detection range of the CCD (Figure S1). To investigate the thermal evolution of these excitonic features, the temperature-dependent PL spectra is analyzed using both the Varshni relation and a semiempirical model, as shown in Figure 4b. The A_{1s} exciton and A^- trion exhibit a characteristic

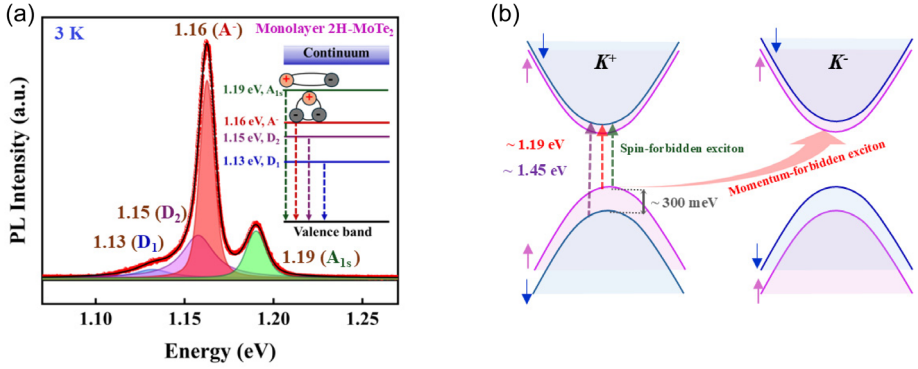

FIGURE 3 | (a) PL spectra of the monolayer at 3 K fitted with Lorentzian (D_1 and D_2) and Voigt functions (A^- and A_{1s}), and the inset is the energy level diagram showing the optical transitions corresponding to the PL spectra. (b) The schematic of K^+ and K^- valley in monolayer, showing the valence band and conduction band splitting.

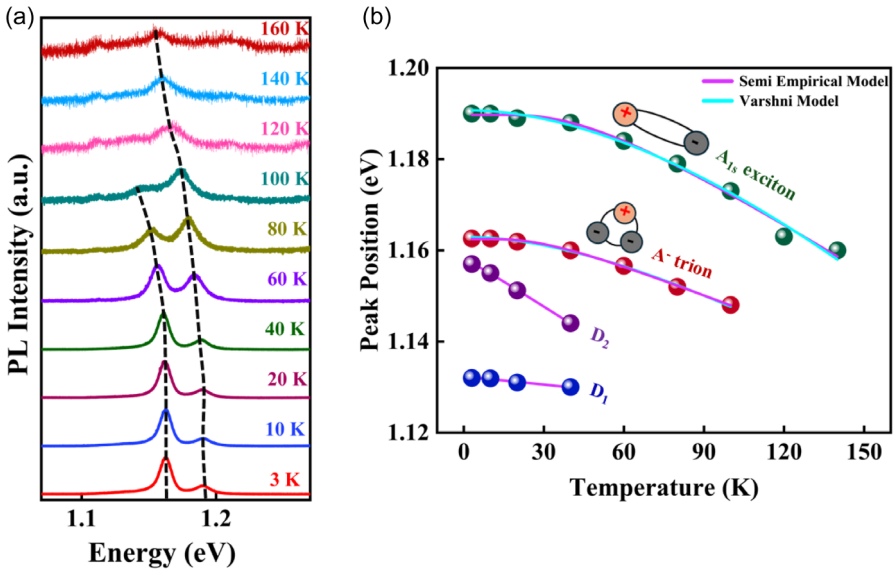

FIGURE 4 | (a) Evolution of the temperate-dependent PL spectra of the monolayer in the range of 3 to 160 K. (b) Temperature-dependent variation of trion and exciton peak positions fitted with both semi empirical formula (Rose) and Varshni equation (Cyan), and D_1 and D_2 with only semiempirical formula.

redshift with increasing temperature, arising from lattice expansion and enhanced electron–phonon interactions [31]. The Varshni equation, which describes the semiconductor bandgap variation with temperature for exciton and trion optical emissions, is expressed as

$$E(T) = E_0 - \frac{\alpha T^2}{\beta + T} \tag{1}$$

where bandgap energy at temperature T is $E(T)$, and at 0 K is E_0, and the α and β are parameters associated with the electron–phonon coupling and Debye temperature, respectively. The fitting parameters for trion is obtained as $E_0 \sim 1.162$ eV, $\alpha \sim 4.4 \times 10^{-4}$, and $\beta \sim 168$ K, respectively. For the A_{1s} exciton, the α value is derived as $\sim 8.45 \times 10^{-4}$ and β value as ~365 K. The Varshni model provides a general trend; a more comprehensive understanding is achieved by considering the exciton–phonon interaction. To understand the exciton–phonon interaction, the data is analyzed with the semi empirical model that is derived from Huang–Rhys theory and proposed by O' Donnel and Chen that accounts for the interaction between excitons and phonons [31]. The model is given by the following equation

$$E = E_0 - S \times E_{\text{ph}} \times \left(\coth\left(\frac{E_{\text{ph}}}{k_B T}\right) - 1 \right) \tag{2}$$

where E_0 is the bandgap at the absolute temperature (0 K), S is the Huang–Rhys factor that gives the exciton–phonon coupling strength, E_{ph} is the average phonon energy, and k_B is the Boltzmann constant. From this fit, the intrinsic bandgap energy of trion at 0 K is extracted as $E_0 \sim 1.162$ eV, which closely matches the lowest measured energy. The average phonon energy involved in the interaction, E_{ph}, is determined to be ~7.7 meV. The Huang–Rhys factor is estimated as $S \sim 1.37$, which quantifies the strength of the exciton–phonon coupling and suggests a significant lattice relaxation upon exciton formation or a strong interaction with a specific phonon mode. By fitting the temperature-dependent variation of the A_{1s} exciton peak position with semiempirical model fit, the extracted parameters are the E_0 ~1.189 eV, $E_{\text{ph}} \sim 12$ meV, and $S \sim 2.2$ and are consistent with previously reported results for monolayer 2H-$MoTe_2$ [29]. The values are relatively lower than the that of other monolayers of Mo-based chalcogenides such as MoS_2 (~19 meV) and $MoSe_2$ (~14.5 meV), suggesting a weaker exciton–phonon coupling in $MoTe_2$ compared to the lighter TMDCs [32]. The longitudinal acoustic phonons in monolayer $MoTe_2$ have energies ranging from 7.4 to 12.5 meV, which is in agreement with the observed results [25]. The E_{ph} values of the peaks D_1 and D_2 are obtained as ~1.1 and ~0.76 meV respectively. The unusually low average phonon energies for the optical transitions suggest they arise from defect-related localized vibrational modes rather than typical optical phonons, reflecting soft lattice distortions induced by vacancies or impurities. The annealing of the TMDC monolayers at higher temperature is known to create the chalcogen vacancies [33, 34]. The chalcogen vacancies in the sulfur-based TMDCs create deep mid-gap states and selenium vacancies create intermediate gap in the photoluminescence spectra. The energy ($\Delta E = E_{X^0} - E_L$) is typically large (100–300 meV), where E_{X^0} is the neutral exciton energy and E_L is the energy of the defect-bound exciton peak. In contrast, for Te-based systems (like $MoTe_2$ or WTe_2), the Te vacancies often result in shallower states due to the smaller electronegativity difference and larger atomic radius of Te, leading to a smaller ΔE (typically 30–60 meV). This can be attributed to the fact that Te has a lower electronegativity compared to sulfur or selenium, which reduces the potential depth of the trap state created by a vacancy consequently the energy separation between the neutral and defect-bound exciton is relatively small [34–36]. Thus, these transitions can be attributed to defect-bound excitons coupled with low-energy phonon modes characteristic of lattice defects.

The PL measurements as a function of excitation laser power have been performed to investigate the nature and origin of

the D_1 peak, which has not been previously reported in the literature. Figure 5a shows the normalized PL spectra as a function of excitation power, and the inset shows the temperature-dependent PL up to 40 K, highlighting the D_1 peak as it vanishes after 40 K. From the power-dependent PL, the D_1 peak saturates at higher power. RIPL, defined as the ratio of the area under each individual peak to the total PL, increases for all transitions except D_1, whose intensity decreases, indicating a declining relative contribution of D_1 to the overall emission (Figure 5b). The FWHM of D1 peak increases with the excitation while that of exciton and trion remains constant as shown in Figure 5c. To rule out the possibility of the transition being of biexciton or neutral exciton, the integrated PL intensity (IPL) of D_1 (I_{D1}) is plotted as a function of IPL of A_{1s} exciton and the data is fitted with power law $I_{D1} \propto I_A^{\alpha}$ (Figure 5d); the value of α is obtained less than 1. The α value of defect-bound exciton is generally sublinear while that for biexciton in TMDCs semiconductors and quantum well systems are typically super linear with values around ~1.2–1.9, and for excitons, it behaves linearly. Thus, the emission peak at 1.132 eV is interpreted as a localized defect-bound excitonic state, based on its low-temperature stability, saturation at high excitation power, and sublinear intensity dependence [37]. The origin of these defects is likely related to the annealing process, which is known to create chalcogen vacancies in TMDCs including $MoTe_2$. In particular, Te vacancies are energetically favorable in $MoTe_2$ and are expected to introduce in-gap states that can bind excitons. The comparative analysis of Raman spectra of the exfoliated monolayer 2H-$MoTe_2$ with and without annealing (untreated) is done and shown in the Supporting Information (Figure S3) to qualitatively understand the presence of disorders. A slight red shift (softening) of A_g^1 and E_{2g}^1 modes is observed in the Raman spectra at room temperature for the annealed monolayer 2H-$MoTe_2$. The linear fit of the A_g^1 and E_{2g}^1 modes with temperature derived the thermal expansion coefficient (TEC) for both samples, as A_g^1 mode is the out-of-plane vibration of the Te atoms and is more sensitive to the introduction of the Te vacancies. The TEC of $\chi_T = -0.0076 \pm 1.8 \times 10^{-4} \mathrm{cm}^{-1}/\mathrm{K}$ is determined for A_g^1 mode of untreated sample which is similar to that reported in the previous study [38]. The TEC of the annealed sample is obtained as $\chi_T = -0.0053 \pm 2.9 \times 10^{-4} \mathrm{cm}^{-1}/\mathrm{K}$ which is comparatively having less negative value than the untreated sample suggesting that the annealing have introduced lattice disorders, favorably Te vacancies that induce the lattice more sensitive to the thermal perturbations.

3 | Conclusion

In this study, we have systematically investigated the excitonic transitions in the monolayer 2H-$MoTe_2$ using temperature-dependent and power-dependent PL measurements. Temperature-dependent PL spectroscopy provides detailed insights into the exciton dynamics and bandgap evolution in this

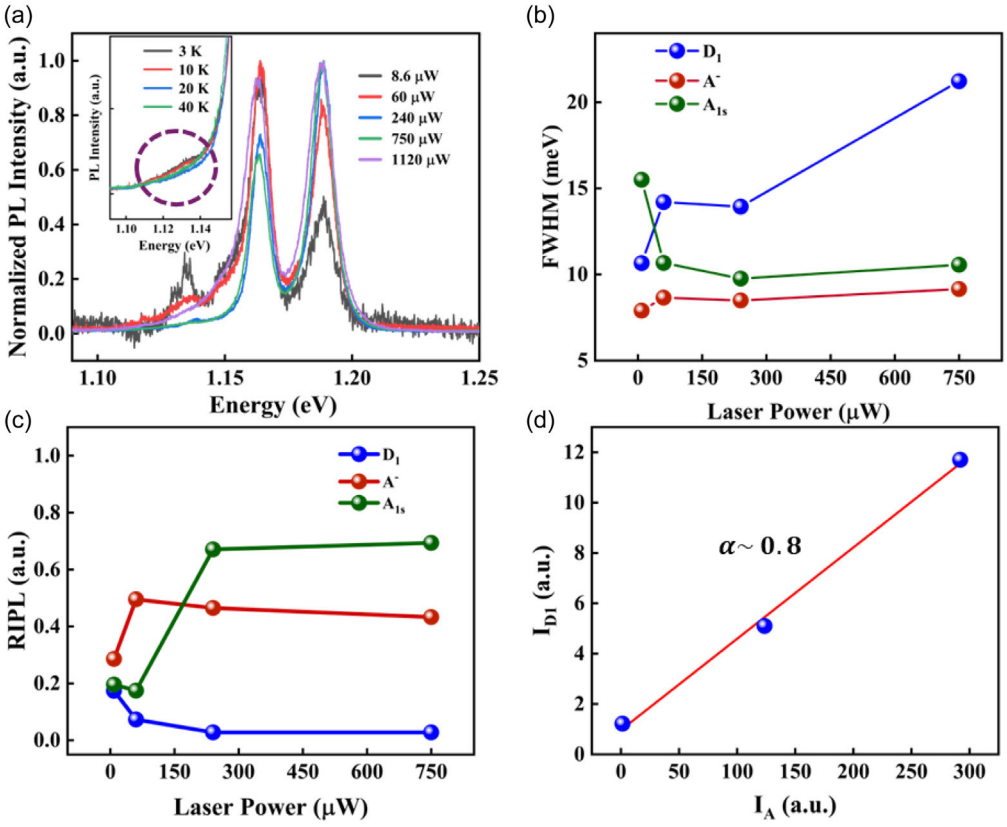

FIGURE 5 | (a) Normalized PL spectra of the D_1 peak as a function of excitation power obtained at 3 K. The inset displays the corresponding temperature-dependent PL measurements over a range of 3 to 40 K. (b) Variation of full width at half maximum (FWHM) of D_1, A^- trion, and A_{1s} exciton transitions with laser power. (c) Laser power dependence of relative integrated PL intensity (RIPL) of D_1, A^- trion, and A_{1s} peaks as a function of laser power. (d) Estimation of sublinear dependence of IPL of D_1 with A_{1s}.

material system. Notably, we identify a previously unreported emission feature at ~1.132 eV, which we attribute to a defect-bound exciton state. The temperature evolution of both excitonic and trionic transition energies is accurately captured using the Varshni relation as well as a semi-empirical model, from which the parameters α and β are extracted to quantify bandgap renormalization. Furthermore, the exciton–phonon coupling strength is determined, highlighting the interactions governing the temperature-driven spectral shifts. Overall, our results deepen the understanding of the temperature-dependent excitonic landscape in monolayer 2H-$MoTe_2$ and shed light on the role of defect-related excitonic states. These findings hold significance for the design and optimization of future optoelectronic, valleytronic, and excitonic devices based on $MoTe_2$ and related two-dimensional materials.

4 | Experimental Section

4.1 | Sample Preparation

The single crystal of 2H-$MoTe_2$ was synthesized by the chemical vapor transport (CVT) technique using tellurium tetrachloride ($TeCl_4$) as the transporting agent. Stoichiometric amounts of commercially available (Sigma–Aldrich) molybdenum (Mo) and tellurium (Te) were mixed in stoichiometric ratios and pressed into a pellet. The pellet was kept at 850°C for 3 days in a box furnace so that Mo and Te will be mixed. The mixture of Mo and Te was then ground together and taken in the quartz ampoule with $TeCl_4$ as a transport additive. Approximately 1 g of polycrystalline powder and $TeCl_4$ ($3 mgcm^{-3}$) were sealed in a quartz ampoule. The ampoule was placed in a tube furnace with the source zone (T_1) maintained at 1000°C and the growth zone (T_2) at 900°C establishing a temperature gradient (ΔT) of 100°C. The well characterized crystal was exfoliated on the SiO_x/Si substrate with ~290 nm SiO_x [39]. The substrates were ultrasonically cleaned sequentially in acetone and isopropanol for 15 min each, followed by immersed in a Piranha solution for 1 h and blow dried with nitrogen (N_2) gas. 2H-$MoTe_2$ flakes were mechanically exfoliated onto the cleaned substrates using the scotch tape method. The exfoliated flakes were subsequently characterized using optical microscopy and Raman spectroscopy.

4.2 | Characterization

The crystal structure and phase purity were analyzed using a Rigaku SmartLab rotating anode diffractometer with $Cu-K\alpha$ radiation ($\lambda = 1.5406$Å). The measurements were performed with a scan rate of ~2 min^{-1} and a step size of 0.02°. Micro-Raman and PL measurements were performed in backscattering configuration using a Horiba Jobin-Yvon LabRAM HR Evolution spectrometer coupled with a Peltier-cooled CCD detector. The system utilized a ~1800 g/mm grating for Raman and a ~600 g/mm grating for PL studies. Room temperature Raman measurements were conducted in a reflection geometry using a 633 nm (1.96eV) excitation laser. To enable the detection of low-frequency vibrational modes, the system was equipped with ultra-low frequency (ULF) filter. Temperature-dependent Raman and PL measurements were carried out using a closed-cycle cryostation manufactured by Montana Instruments. The resulting PL spectra were analyzed by fitting the peaks with Lorentzian and Voigt functions.

Acknowledgments

The authors would like to acknowledge IIT Mandi for the research facility. A.S. would like to thank Anusandhan National Research Foundation, New Delhi, India, for the project with grant number ANRF/ARG/2025/001724/PS.

Conflicts of Interest

The authors declare no conflicts of interest.

Data Availability Statement

The data that support the findings of this study are available from the corresponding author upon reasonable request.

References

1. K. S. Novoselov, A. K. Geim, S. V. Morozov, et al., "Electric Field Effect in Atomically Thin Carbon Films," *Science* 306 (2004): 666–669.

2. Y. Zhang, Y.-W. Tan, H. L. Stormer, and P. Kim, "Experimental Observation of the Quantum Hall Effect and Berry's Phase in Graphene," *Nature* 438 (2005): 201–204.

3. P. Ho, "Twenty Years of 2D Materials,"*Nature Physics* 20 (2024): 1–1.

4. S. Manzeli, D. Ovchinnikov, D. Pasquier, O. V. Yazyev, and A. Kis, "2D Transition Metal Dichalcogenides," *Nature Reviews Materials* 2 (2017): 17033.

5. C. J. Ciccarino, T. Christensen, R. Sundararaman, and P. Narang, "Dynamics and Spin-Valley Locking Effects in Monolayer Transition Metal Dichalcogenides," *Nano Letters* 18 (2018): 5709–5715.

6. J. Xiao, Z. Ye, Y. Wang, et al., "Nonlinear Optical Selection Rule Based on Valley-Exciton Locking in Monolayer WS_2," *Light: Science and Applications* 4 (2015): e366–e366.

7. T. Cao, G. Wang, W. Han, et al., "Valley-Selective Circular Dichroism of Monolayer Molybdenum Disulphide," *Nature Communications* 3 (2012): 887.

8. G. Aivazian, Z. Gong, A. M. Jones, et al., "Magnetic Control of Valley Pseudospin in Monolayer WSe_2," *Nature Physics* 11 (2015): 148–152.

9. D. Xiao, G.-B. Liu, W. Feng, X. Xu, and W. Yao, "Coupled Spin and Valley Physics in Monolayers of MoS_2 and Other Group-VI Dichalcogenides," *Physical Review Letters* 108 (2012): 196802.

10. T. Handa, M. Holbrook, N. Olsen, et al., "Spontaneous Exciton Dissociation in Transition Metal Dichalcogenide Monolayers," *Science Advances* 10 (2024): eadj4060.

11. C. Ruppert, B. Aslan, and T. F. Heinz, "Optical Properties and Band Gap of Single- and Few-Layer $MoTe_2$ Crystals," *Nano Letters* 14 (2014): 6231–6236.

12. E. Jung, J. C. Park, Y.-S. Seo, et al., "Unusually Large Exciton Binding Energy in Multilayered 2H-$MoTe_2$," *Scientific Reports* 12 (2022): 4543.

13. R. Oliva, T. Woźniak, F. Dybala, et al., "Hidden Spin-Polarized Bands in Semiconducting 2H-$MoTe_2$," *Materials Research Letters* 8 (2020): 75–81.

14. M. Yamamoto, S. T. Wang, M. Ni, et al., "Strong Enhancement of Raman Scattering from a Bulk-Inactive Vibrational Mode in Few-Layer $MoTe_2$," *ACS Nano* 8 (2014): 3895–3903.

15. S. Biswas, A. Champagne, J. B. Haber, et al., "Rydberg Excitons and Trions in Monolayer $MoTe_2$," *ACS Nano* 17 (2023): 7685–7694.

16. B. Chen, H. Sahin, A. Suslu, et al., "Environmental Changes in $MoTe_2$ Excitonic Dynamics by Defects-Activated Molecular Interaction," *ACS Nano* 9 (2015): 5326–5332.

17. M. Grzeszczyk, K. Gołasa, M. R. Molas, et al., "Raman Scattering from the Bulk Inactive Out-of-Plane $B_{2g}{}^1$ Mode in Few-Layer $MoTe_2$," *Scientific Reports* 8 (2018): 17745.

18. S. Koirala, S. Mouri, Y. Miyauchi, and K. Matsuda, "Homogeneous Linewidth Broadening and Exciton Dephasing Mechanism in $MoTe_2$," *Physical Review B* 93 (2016): 075411.

19. Y. Lei, Q. Lin, S. Xiao, J. Li, and H. Fang, "Optically Active Telecom Defects in $MoTe_2$ Fewlayers at Room Temperature," *Nanomaterials* 13 (2023): 1501.

20. J. Yang, T. Lü, Y. W. Myint, et al., "Robust Excitons and Trions in Monolayer $MoTe_2$," *ACS Nano* 9 (2015): 6603–6609.

21. J. P. Echeverry, B. Urbaszek, T. Amand, X. Marie, and I. C. Gerber, "Splitting between Bright and Dark Excitons in Transition Metal Dichalcogenide Monolayers," *Physical Review B* 93 (2016): 121107.

22. D. Puotinen and R. E. Newnham, "The Crystal Structure of $MoTe_2$," *Acta Crystallographica* 14 (1961): 691–692.

23. J. Park, Y. Kim, Y. I. Jhon, and Y. M. Jhon, "Temperature Dependent Raman Spectroscopic Study of Mono-, Bi-, and Tri-Layer Molybdenum Ditelluride," *Applied Physics Letters* 107, 2015.

24. D. Rawat, A. Singh, N. K. Singh, and A. Soni, "Anisotropic Light-Matter Interactions in the Single-Crystal Topological Insulator Bismuth Selenide," *Physical Review B* 107 (2023): 155203.

25. H. Guo, T. Yang, M. Yamamoto, et al., "Double Resonance Raman Modes in Monolayer and Few-Layer $MoTe_2$," *Physical Review B* 91 (2015): 205415.

26. A. C. Ferrari and D. M. Basko, "Raman Spectroscopy as a Versatile Tool for Studying the Properties of Graphene," *Nature Nanotechnology* 8 (2013): 235–246.

27. X. Zhang, W. P. Han, J. B. Wu, et al., "Raman Spectroscopy of Shear and Layer Breathing Modes in Multilayer MoS_2," *Physical Review B* 87 (2013): 115413.

28. A. Arora, R. Schmidt, R. Schneider, et al., "Valley Zeeman Splitting and Valley Polarization of Neutral and Charged Excitons in Monolayer $MoTe_2$ at High Magnetic Fields," *Nano Letters* 16 (2016): 3624–3629.

29. S. Helmrich, R. Schneider, A. W. Achtstein, et al., "Exciton–phonon Coupling in Mono- and Bilayer $MoTe_2$," *2D Materials* 5 (2018): 045007.

30. C. Robert, R. Picard, D. Lagarde, et al., "Excitonic Properties of Semiconducting Monolayer and Bilayer $MoTe_2$," *Physical Review B* 94 (2016): 155425.

31. K. P. O'Donnell and X. Chen, "Temperature Dependence of Semiconductor Band Gaps," *Applied Physics Letters* 58 (1991): 2924–2926.

32. G. Kioseoglou, A. T. Hanbicki, M. Currie, A. L. Friedman, and B. T. Jonker, "Optical Polarization and Intervalley Scattering in Single Layers of MoS_2 and $MoSe_2$," *Scientific Reports* 6 (2016): 25041.

33. E. Mitterreiter, B. Schuler, A. Micevic, et al., "The Role of Chalcogen Vacancies for Atomic Defect Emission in MoS_2," *Nature Communications* 12 (2021): 3822.

34. E. Żuberek, J. Olejnik, J. Debus, et al., "Photon Upconversion of Defect-Bound Excitons in hBN-Encapsulated MoS_2 Monolayer," *The Journal of Physical Chemistry C* 128 (2024): 19288–19296.

35. Y. Zhu, J. Lim, Z. Zhang, et al., "Room-Temperature Photoluminescence Mediated by Sulfur Vacancies in 2D Molybdenum Disulfide," *ACS Nano* 17 (2023): 13545–13553.

36. S. A. Kazemi, S. Imani Yengejeh, S. A. Ogunkunle, et al., "Vacancy Impacts on Electronic and Mechanical Properties of MX_2 (M = Mo, W and X = S, Se) Monolayers," *RSC Advances* 13 (2023): 6498–6506.

37. J. Pandey and A. Soni, "Unraveling Biexciton and Excitonic Excited States from Defect Bound States in Monolayer MoS_2," *Applied Surface Science* 463 (2019): 52–57.

38. W. Wang, C. Wang, Y. Chen, et al., "Anharmonic Phonon Scattering Study of 2H–$MoTe_2$ Crystal by Raman Spectroscopy," *Solid State Communications* 379 (2024): 115423.

39. D. H. Keum, S. Cho, J. H. Kim, et al., "Bandgap Opening in Few-Layered Monoclinic $MoTe_2$," *Nature Physics* 11 (2015): 482–486.

Supporting Information

Additional supporting information can be found online in the Supporting Information section. **Supporting Fig. 1:** Temperature dependent PL spectra 3 to 300 K. **Supporting Fig. 2:** Temperature dependent PL spectra of (a) monolayer 2H $MoTe_2$, and (b) SiO_2/Si substrate. **Supporting Fig. 3:** (a) Raman spectra of untreated (blue) and annealed (red) samples at room temperature, and (b) temperature-dependent evolution of phonon frequencies for both samples. The first-order temperature coefficients are determined for both A_g^1 and E_{2g}^1 modes.